The 2021 volcanic eruption in La Palma Island and its impact on ionospheric scintillation as measured from GNSS reference stations, GNSS-R, and GNSS-RO

Carlos Molina[1], Badr-Eddine Boudriki Semlali[1], Guillermo González-Casado[2], Hyuk Park[1,3], and Adriano Camps[1,3,4]

[1]CommSensLab – UPC, Universitat Politècnica de Catalunya – BarcelonaTech, 08034 Barcelona, Spain
[2]Research Group of Astronomy and Geomatics (gAGE) - UPC, 08034 Barcelona, Spain
[3]IEEC-Institut d'Estudis Espacials de Catalunya, 08034 Barcelona, Spain
[4]ASPIRE Visiting International Professor at UAE University, CoE, PO Box 15551, Al Ain, Abu Dabhi, U.A.E.

Correspondence: Carlos Molina (carlos.molina@upc.edu)

Abstract. Ionospheric disturbances induced by seismic activity have been studied in the last years by many authors, showing an impact both before and after the occurrence of earthquakes. In this study, the ionospheric scintillation produced by the 2021 La Palma volcano eruption is analyzed. The "Cumbre Vieja" volcano was active from 19 September to 13 December 2021, and many magnitude 3-4 earthquakes were recorded, with some of them reaching magnitude 5. Three methods: GNSS reference monitoring, GNSS Reflectometry (GNSS-R) from NASA CYGNSS, and GNSS Radio Occultation (GNSS-RO) from COSMIC and Spire constellations are used to compare and evaluate their sensitivity as proxies of earthquakes associated with the volcanic eruption. To compare the seismic activity with ionospheric scintillation, ~~earthquakes' generated energy~~ seismic energy release, and percentile 95 of the intensity scintillation parameter (S_4), measurements have been computed every 6 h intervals for the whole duration of the volcanic eruption. GNSS-RO has shown the best correlation between earthquakes' energy and S_4, with values up to 0.09 when the perturbations occur around 18 h after the seismic activity. GNSS reference monitoring stations data also shows some correlation 18 h after and 7-8 days after. As expected, GNSS-R is the one that shows the smallest correlation, as the ionospheric signatures get masked by the signature of the surface where the reflection is taking place. Additionally, the three methods show a smaller correlation during the week before earthquakes, even though, given the small magnitude of the seismic activity, the correlation is barely detectable in this situation, and difficult to use in any application to find earthquake proxies.

1 Introduction

Ionospheric disturbances such as scintillation constitute a notable problem for satellite communications, global navigation satellite systems (GNSS), and Earth observation systems, notably at P and L-bands. They can disturb the signals making it difficult or even impossible to transmit the correct information through the ionosphere. Nevertheless, they can also be seen as an opportunity to detect, measure, or infer other physical phenomena, not necessarily related to the ionosphere itself. For example, in the last decades, several studies have shown that ionospheric disturbances can occur during solar eclipses (Das

et al., 2022), or geomagnetic storms (Ding et al., 2007; Li et al., 2008), which are due to causes external to the Earth, coming from the Sun or near space weather.

~~In addition, other "~~Recent evidence shows that the ionosphere may also be impacted by other "internal~~" causes have recently shown that they can impact the ionosphere too~~" geophysical events. There are studies relating severe atmospheric phenomena such as cyclones or hurricanes to ionospheric anomalies ~~(??Kamogawa, 2006)~~(Kamogawa, 2006; Camps et al., 2018; Xu et al., 2019). Anomalous variations in the Total Electron Content (TEC) and peaks in the ionospheric scintillation have been detected during the passage of a large cyclone or hurricane, ~~which creates~~ generating gravity waves that couple to the lower ionosphere, yielding to ionospheric disturbances.

Another source of perturbations in the ionosphere is related to the ~~lithosphere, and the seismic activity~~ seismic activity within the lithosphere, as supported by many studies that ~~are being~~ have been published in the last years by (Liu et al., 2004; Pulinets, 2004; Kamogawa, 2006; Pulinets and Davidenko, 2014; Pulinets et al., 2021; Molina et al., 2021, 2022). The physical mechanisms behind this interaction are still not very clear, but there are several research paths open. Some of them explain this interaction by the generation of low-frequency electromagnetic signals from the underground rock under huge pressures during the earthquake preparation period. Other authors explain the interaction by changes in the surface electric potential due to the piezoelectric effect in the underlying rocks, which can induce changes in the ionosphere's TEC.

This study looks for ionospheric anomalies related to the seismic activity generated by a recent volcano eruption on the Spanish island of La Palma (Canary Islands). ~~In the past, other~~ Past studies have analyzed the impact of volcanic eruptions on the ionosphere (De Ragone et al., 2004; Shults et al., 2016; Astafyeva, 2019; Yong-Qiang et al., 2006). For example, the recent Tonga submarine eruption on 12 January 2022 created traveling ionospheric disturbances (TID) from the eruption site (Themens et al., 2022). ~~In this case, the~~ The Tonga eruption was so strong that the gravity waves generated within the atmosphere traveled to the ionosphere, and then propagated concentrically all around the globe producing these perturbations. ~~The~~ While the 2021 La Palma eruption ~~that happened last year, wasn't as explosive as the Tonga one, but it was much longer in time, and~~ was less explosive than the Tonga eruption, it ~~occurred over a longer period and~~ had significant seismic activity ~~associated with it~~leading up to and over the duration of the event.

1.1 The September 2021 "Cumbre Vieja" Volcanic eruption in La Palma (Spain)

La Palma is a volcanic island located in the ~~North West~~ northwest of the Canary Islands archipelago (Spain) in the Atlantic Ocean, at ~500 km from the coast of Africa. The island has relatively low volcanic activity with only three eruptions in the last century ~~,~~ and seven in the last 500 years~~, even though it~~. Even with infrequent eruptions, La Palma is one of the ~~islands in the archipelago~~archipelago islands with the highest potential risks (Fernández et al., 2021).

The last eruption started at 13:43 UTC on 19 September 2021, near the former volcano "Cumbre Vieja", and it lasted for 85 days until 13 December 2021, when it was declared finished.

Preceding the eruption, for eight days since 11 September a series of earthquakes were registered in the region where the eruption took place.

55 Around 6000 earthquakes occurred during this time frame with magnitudes ranging from 1mbLg to 3.8 mbLg (mbLg is the magnitude unit used by the Instituto Geográfico Nacional (IGN) to characterize the earthquakes on the island, and it is equivalent to the local Ritcher magnitude for a distance of 100 km). In this period, the epicenters migrated North, approaching ~~to~~ the eruptive cone location, at the same time as the ~~hipocenter~~ hypocenter depths rose starting from 15 km below the surface to near-surface depths. The evolution of the locations and depths of this precursory earthquake swarm is shown in Fig. 1.
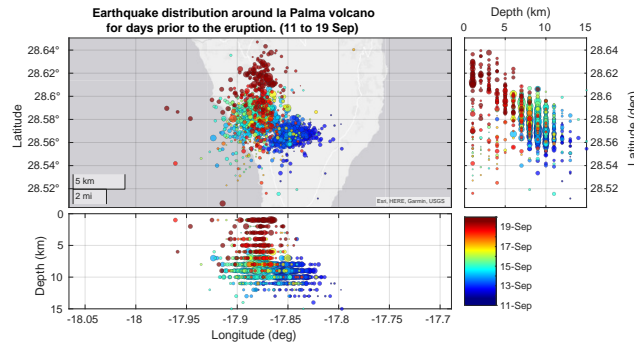
Figure 1. Series of earthquakes preceding the volcanic eruption from 11 September indicating their position, depths, and date.

60 During the 10 days following the start of the eruption, while the lava, gasses, and ashes were being expelled from the volcano, the seismic activity was relatively low. At the ~~begging~~ beginning of October, around 15 days after the start of the eruption, the seismic activity increased again and ~~remain~~ remained stable until the end of the eruption, which was declared ~~to be~~ on 13 December.

2 Data sources and methods

65 This study is focused on the simultaneous analysis of several sources of data measuring the ionospheric scintillation with GNSS signals and correlating them with the seismic activity related to the eruptive event in La Palma in 2021.

 ~~The same physical mechanism is involved in the three techniques used~~ Global Navigation Satellite Systems (GNSS) are systems that can provide precise geolocation on the Earth by using the electromagnetic signal received from several satellites at a point. Current GNSS networks are the American GPS, Russian GLONASS, European Galileo, and Chinese BeiDou. To

70 ensure global coverage, they are composed of a satellite constellation of 18 to ~~measure the ionospheric scintillation through GNSS signals, and it is based~~ 30 medium Earth orbit (MEO) satellites, with orbital periods of about 12 hours. During the last decades, the signal coming from these satellites has proved to be very useful in doing remote sensing of the Earth and study properties such as soil moisture (Rodriguez-Alvarez et al., 2009), sea ice thickness (Munoz-Martin et al., 2020), wave height and roughness (Wang et al., 2022).

75 GNSS signals are also handy for studying the ionosphere. As these signals pass through the ionosphere, they undergo effects like bending, delay, and absorption. These effects help us learn about ionospheric properties, such as Total Electron Content (TEC) and ionospheric scintillation (Shanmugam et al., 2012; Camps et al., 2018; Angling et al., 2021). In this study,

we've used three methods to measure ionospheric scintillation using GNSS signals. All these methods rely on the fact that disturbances in the ionosphere's electron density affect how GNSS signals propagate, especially in their frequency bands.

Ionospheric scintillation refers to the rapid fluctuations in phase and/or intensity of the electromagnetic signal received after crossing the ionosphere. From now on, the study will be centered only on the intensity, also called "amplitude scintillation". It is usually measured as the normalized standard deviation of the intensity of a radio electromagnetic signal after crossing the ionosphere, and it is computed with eqn. 1.

$$S_4 = \sqrt{\frac{\langle I^2 \rangle - \langle I \rangle^2}{\langle I \rangle^2}}, \tag{1}$$

where I is the signal's intensity, and $\langle \cdots \rangle$ represents the average of a certain period, usually in the order of tens of seconds.

The three GNSS-related techniques used to measure ionospheric amplitude scintillation are (1) static ground-based GNSS reference monitoring, (2) GNSS-R (GNSS Reflectometry), and (3) GNSS-RO (GNSS Radio Occultation). The novelty and interest of this work come from the analysis of the effects that the same physical phenomenon, a volcanic eruption, produces in the ionosphere, as observed by three different techniques measuring the same magnitude at the same frequency.

2.1 Ground stations data

Ground-based GNSS stations continuously monitor the signals emitted by GNSS satellites, providing valuable TEC and scintillation data used to make ionospheric corrections for navigation and to assess the quality of the service.

One disadvantage of this technique is the sparse spatial coverage compared to other satellite-based techniques. GNSS stations are typically sparsely installed at fixed ground locations, only providing data for the local region. Fortunately for this study, there are two ground stations close to the volcano. One station is located on the same island (La Palma), which from now on, will be identified as LPAL, and the second one is in Maspalomas (MAS1), a town South of the Gran Canaria Island, which is around 250 km southeast of the volcano. Figure 2 shows a map displaying the two ground stations.

The GNSS monitoring ground station data contains the measurement for every minute of all the GNSS satellites in view for each station (Juan et al., 2018; Rovira-Garcia et al., 2020). The database has been pre-processed using the algorithms described in (Juan et al., 2017), which includes the variables listed in Table 1:

The S_4 data here is obtained by using eqn. 1 averaging over a period of 1 minute and using the direct intensity received in ground stations from the GNSS satellites in view.
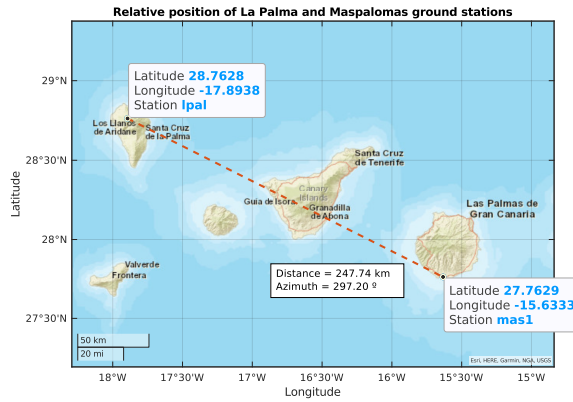
Figure 2. Relative position of LPAL and MAS1 ground stations with respect to the La Palma Island, which is the top left one. Map: Esri, HERE, Garmin, NGA, USGS.

Table 1. GNSS monitoring ground stations database variables

Variable Name	Description
Year	Year of the measurement
DoY	Day of the Year
Seconds	Second of the day
Satellite	Satellite number
	1 to 33: GPS
	37 to 70: GLONASS
	71 to 120: GALILEO
	121+: discarded
Azimuth (deg)	Azimuth from the station (North at 0º)
Elevation (deg)	Elevation from the station (0º – 90º)
S4	Amplitude scintillation calculated over 60 s
Sigma_phi	σ_ϕ from the L1 signal calculated over 60 s

A clear trend between the elevation angle and the measured scintillation has been observed. The smaller the elevation angle, the larger the S_4, which can be attributed to the longer path within the ionosphere of the lower elevation rays, which may suffer

5

from stronger scintillation and multipath propagation. This behavior is displayed in Fig. 3. Therefore, data with an elevation lower than 30º has been discarded.
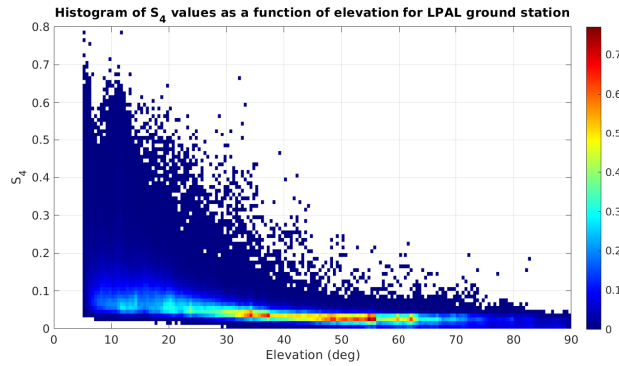

Figure 3. Histogram of S_4 values with respect to the elevation angle for La Palma ground station data.
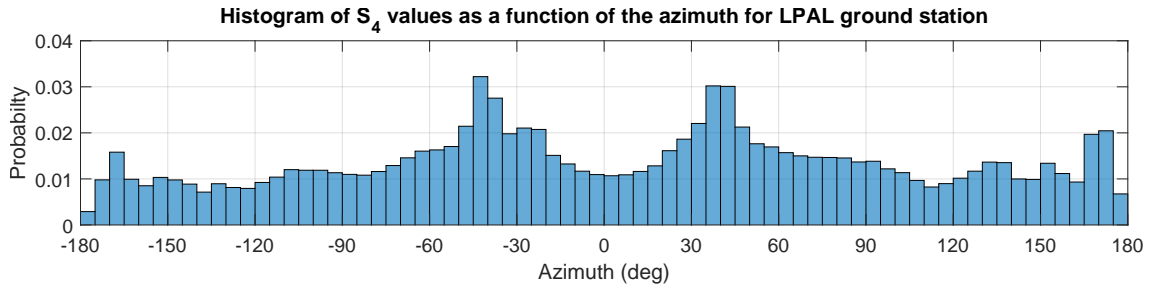

Figure 4. Histogram of the amount of S_4 measurements as a function of the azimuth.

Also, the dependence on azimuth has been studied. A certain dependence of the number of measurements vs. the azimuth has also been found. As shown in Fig. 4, the most probable azimuths for receiving GNSS signals at the LPAL station are +45º and -45º.

Figure 5 shows the percentile 95% of S_4 values as a function of time and azimuth, and it can be observed that the largest values are obtained, for both stations, mostly when the GNSS satellites are located southwards, near 180º azimuth.

2.2 GNSS-R data

GNSS-Reflectometry has also proven to be a good way to detect ionospheric scintillation over calm oceanic regions (Molina and Camps, 2020). The open-access NASA CYGNSS GNSS-R constellation, which started providing science data in March 2017, was utilized for this study. CYGNSS orbit's inclination is around 35º, so the coverage is from 40ºS to 40ºN, which includes the latitude of the islands (28.5ºN).
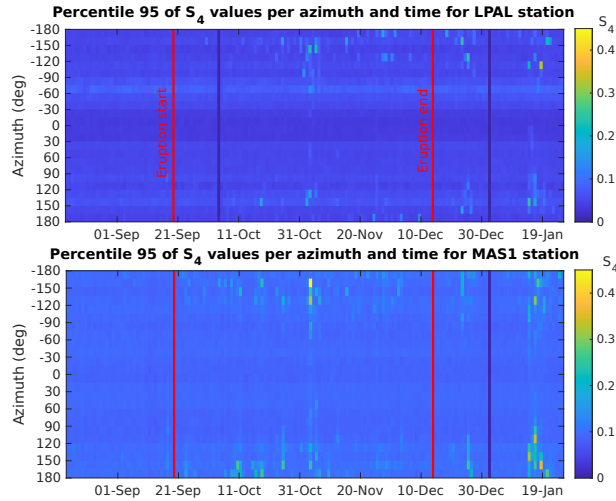
Figure 5. Percentile 95% of S_4 values as a function of the azimuth (in the vertical axis) and time (in the horizontal axis) for LPAL and MAS1 ground stations respectively, where it can be observed that most of the S_4 peaks are detected around the South direction.
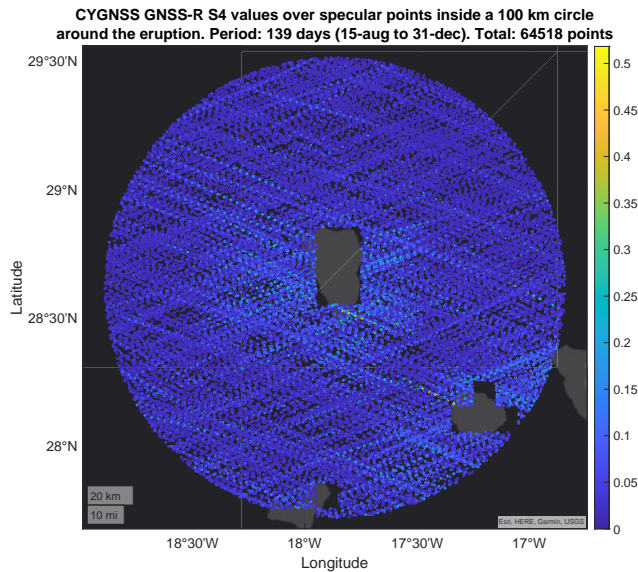

Figure 6. Position of CYGNSS GNSS-R specular reflection points inside a circle of 100 km around La Palma Island for the whole period studied, indicating the S_4 in colors. Map: Esri, HERE, Garmin, USGS.

The eight satellites comprising the CYGNSS constellation are continuously tracking up to 4 GPS satellites in view, taking measurements at a sample rate of 2 Hz, providing good availability of data in the region close to La Palma. During the full 139-day eruptive period, about 65 000 points were recorded within a radius of 50 km around the island.

7

The location of each point corresponds to the specular reflection point of each trajectory between the GPS satellite and the CYGNSS receiver, as shown in Fig. 6. The ~~track of these reflected signals~~signals' path crosses the ionosphere twice because the height of the CYGNSS satellites is around 520 km, which is above the typical height of the ionosphere's maximum density

130   (~350 km). ~~As~~ The receiver GNSS-R instrument cannot distinguish if the scintillation was generated in the ascending or descending paths, or in a combination of both, therefore we have used the specular reflection point ~~is used to locate the~~ to tag the scintillation measurements.

GNSS-R data has been processed following the methodology detailed in (Molina and Camps, 2020), doing the moving average and standard deviation of the SNR for a 10 s window, and computing the S_4 index with eqn. 1, in which I has been

135   computed from the SNR of the Delay Doppler Map (DDM) of the CYGNSS product.

As the performance of the GNSS-R technique to estimate the scintillation is affected by the sea surface roughness, another filter has been applied. A wavy water surface destroys the signal coherence, making it impossible to infer the scintillation suffered along the path. Using data from maritime buoys around the islands, the model SIMAR detailed in Puertos del Estado (2020) documentation extrapolates the wave height in a grid of points along the ocean. Figure 7 shows the position of these

140   points around La Palma Island and the ones selected to estimate the wave height during the eruptive period. The wave height extracted from them is compared to the detected scintillation from CYGNSS in Fig. 8. It can be observed that the high values of scintillation can appear only when the sea roughness is small, as indicated by the color-shaded areas. For example, the peaks around 4 September appear during a period of waves lower than 1.5 m. Similar behavior is observed around 25 September, 16 October, or 2 November.

Figure 7. Set of SIMAR model points around the island, indicating the ones selected to extract the Significant Wave Height (SWH) around La Palma. Dataset downloaded from Puertos del Estado (2022) website. Map: Sentinel-2 cloudless 2021 by EOX IT Services GmbH.

145   Figure 9 shows the comparison between the Significant Wave Height (SWH) in the horizontal axis vs. the detected value of S_4, confirming what was observed in the timeline in Fig. 8. In this correlation, we can define a noise floor at 0.02 to remove all the values that are prone to be affected by the sea surface roughness. In the study, we compare the results for both cases: when using all data without filtering and when using only S_4 values above 0.02.
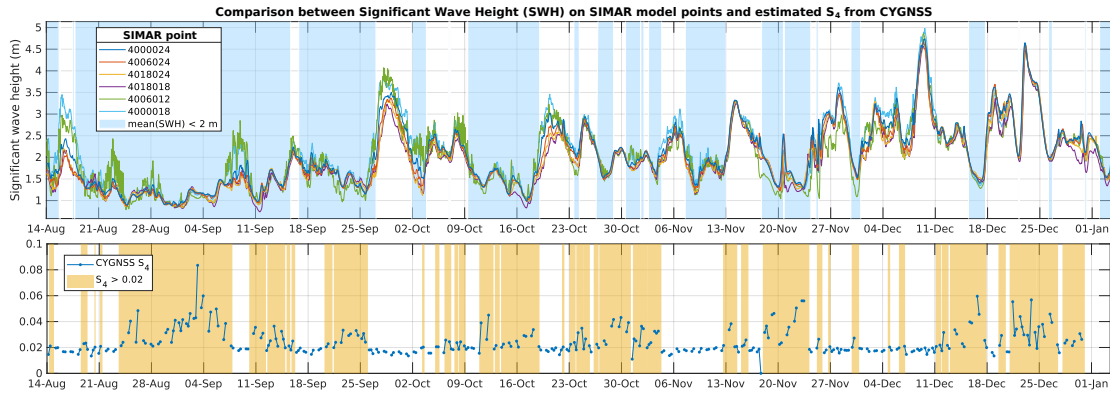
Figure 8. Significant Wave Height (SWH) from 6 SIMAR model points every hour around La Palma, compared to the estimated S_4 from CYGNSS GNSS-R data. Light blue shaded area marks the periods with an average SWH less than 2 m and the yellow area marks the intervals in which the S_4 is larger than 0.02, showing that most of the S_4 peaks ~~only~~ typically appear when the SWH is low.
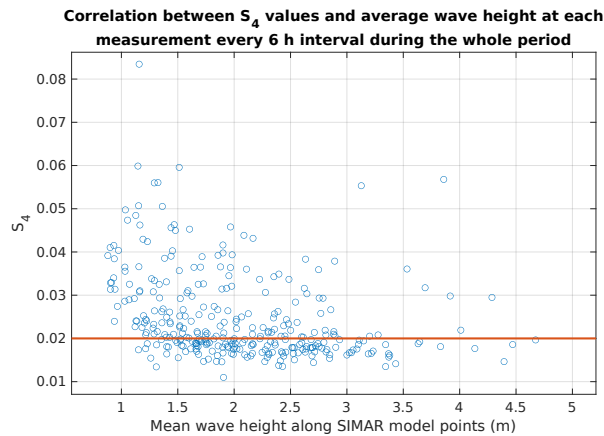

Figure 9. Correlation between the wave height and the detected scintillation index S_4 using GNSS-R from CYGNSS.

2.3 GNSS-RO data

150   The GNSS Radio-Occultation method is another way to retrieve information about the ionosphere using GNSS signals. In this case, the signal emitted by the GNSS satellites is received by the receiver onboard a LEO satellite when they are setting under or rising above the horizon. The use of this technique has the advantage of not being affected by ground reflection disturbances as in GNSS-R. For the same reason, land and oceanic regions can be studied indistinctly.

For this study, Spire and open-access data from COSMIC-2 (UCAR/NCAR, 2019) have been used. Spire Global (Jales et al.,
155   2020; Irisov et al., 2018) operates a constellation of more than 80 3U CubeSats that can perform GNSS-RO, and more recently

GNSS-R as well. From Spire, measurements from around 58 000 GNSS-RO occultations in the region around La Palma Island from 15 August to 31 October 2019 have been used.

Cosmic data includes all the occultations of GPS satellites as seen from the constellation of COSMIC-2 LEO satellites. COSMIC-2, also known as FORMOSAT-7, is a constellation of 6 LEO mini-satellites (300 kg) that were launched on 25 June 2019 into a 24º inclination orbit. The Level 1b podTc2 dataset contains the information used in this study, which is detailed in Table 2.

Table 2. Level 1b "podTc2" database variables available from COSMIC-2 database.

Variable Name	Description
Time (GPS seconds)	GPS time of the measurements (seconds from 1 Jan 1980)
TEC (TECU)	Total Electron Content along LEO-GPS link (slant TEC)
caL1_SNR (V/V)	Signal to Noise ratio on the L1 channel, CA code
pL2_SNR (V/V)	Signal to Noise Ratio on the L2 channel, P code
x_LEO (km) y_LEO (km) z_LEO (km)	LEO position (ECF) at time of signal acquisition.
x_GPS (km) y_GPS (km) z_GPS (km)	GPS position (ECF) at time of signal acquisition.
S4	S_4 scintillation index

With these data, the tangent point, (i.e., the point in the trajectory which is closer to the Earth), can be computed from the GPS and LEO satellite positions. For each of these points, the corresponding S_4 value has been computed, and their coordinates will be used later to filter by the distance around the volcano. Given that the occultations have been recorded during long periods, including high elevation angles (almost 90º in some cases), it is proposed a method to filter the data points that correspond to the rays traversing the ionosphere.
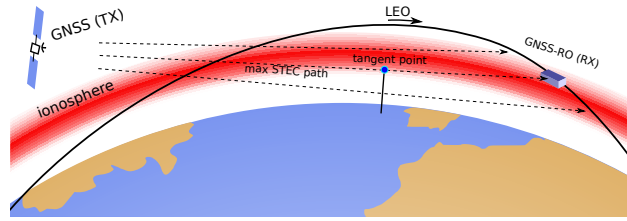
Figure 10. Schematics of the GNSS-RO technique to measure the ionosphere, indicating the location of the tangent point in the path with maximum STEC value.
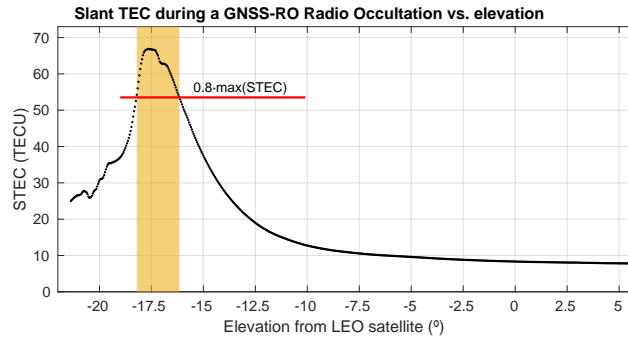

Figure 11. STEC variation during a GNSS occultation as a function of the elevation angles seen from a COSMIC-2 satellite on 19 September 2021.

Using the slant TEC (STEC) value during the occultation, we can assume that the maximum value coincides with the path in which the ray crosses its longest path in the ionosphere, as shown in Fig. 10. Selecting the points that have a STEC larger than 80% of the maximum TEC in each occultation leaves the points that are inside the ionosphere, more likely to suffer from scintillation, as ~~show~~ shown in Fig. 11.

Figure 12 shows the location of the points with STEC larger than ~~the~~ 80% of the maximum one and within a circle of 1000 km radius around the eruption coordinates.

2.4 Seismic activity data

The database of earthquakes has been retrieved from the Spanish Instituto Geográfico Nacional (IGN) (2022). For the whole duration of the eruption, around 9200 earthquakes have been recorded in the database, which includes information about their time, magnitude, location, and depth.

Earthquakes are represented in Fig. 13, indicating their depth in the vertical axis during the whole eruption period (yellow shade). As observed in the figure, there is a precursor seismic activity close to the surface with decreasing depths, then a relatively calm period of ~~8 days~~ 8 days, preceding a roughly stable activity with earthquakes at two differentiated depths, but
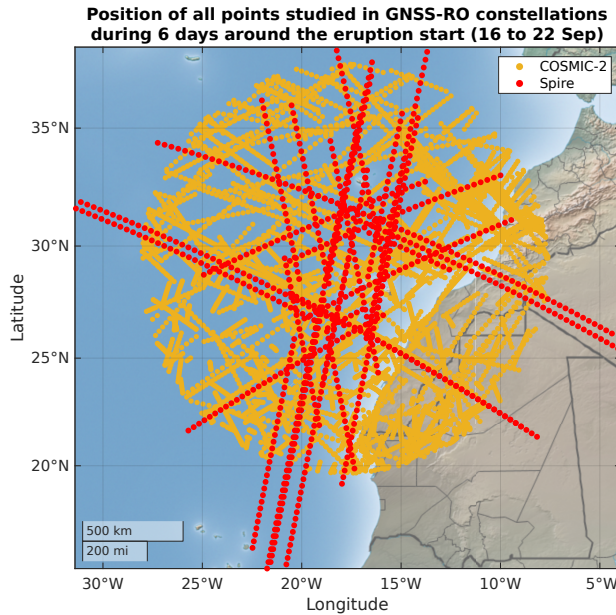
11

Figure 12. Location of Spire (in red) and COSMIC-2 (in yellow) measurements during 6 days (±3 days) around the start of the volcanic eruption on 19 September. Map: made with Natural Earth.

180　with homogeneous magnitudes in each group. When the eruption ~~ends~~ended, the seismic activity lasted for approximately 15 more days with decreasing magnitude and frequency.
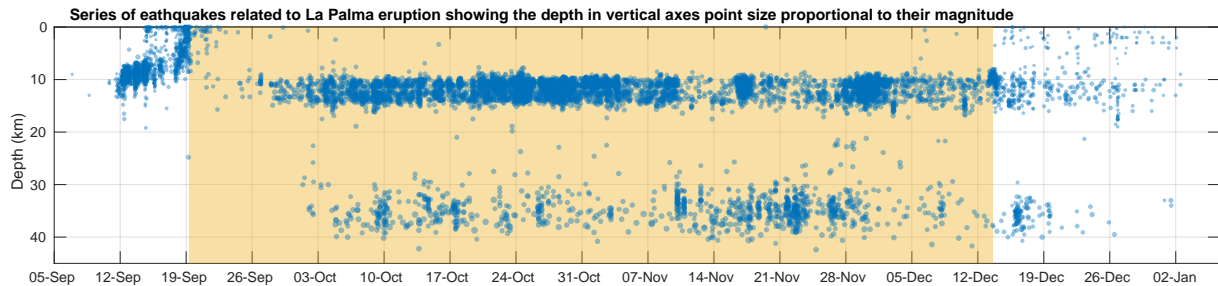

Figure 13. Series of earthquakes associated with the volcanic eruption in La Palma Island, indicating their depth in the vertical axis, and their magnitude proportional to the point size. The volcanic eruption is active during the period shaded in yellow.

　　To allow the comparison between the seismic activity and the corresponding ionospheric scintillation indicator, it is proposed to use the ~~energy generated~~ seismic energy released per earthquake and then integrate all the earthquakes' energy in a time interval. The rationale behind the selection of these metrics is that, whichever mechanism is involved in the perturbation of the

12

ionosphere, the larger the energy dissipated into the environment, the larger the induced perturbations should be. The formula used to compute the energy per earthquake is taken from the work of (Gutenberg and Richter, 1955):

$$\log E = 5.8 + 2.4m, \tag{2}$$

where m is the magnitude of the earthquake, and E is the dissipated energy in Ergs.

Figure 14 shows a temporal histogram of the magnitude of earthquakes during the eruption period, indicating in ~~vertical~~ the vertical axis the magnitude, and in colors the number of earthquakes per bin. Red arrows mark the beginning and end of the eruption, respectively. The orange line represents the integrated energy every 6-hour intervals, computed for each earthquake using eqn. 2.
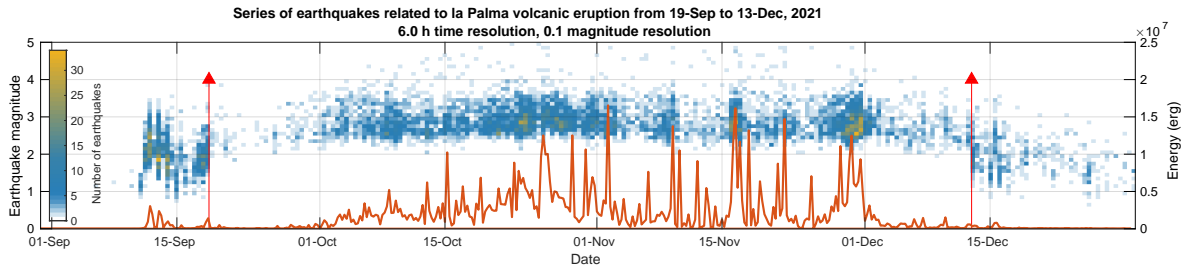

Figure 14. Seismic activity associated with the La Palma volcano eruption for the whole period, showing in colors the histogram of magnitudes and the integrated ~~generated~~ seismic energy with an orange line. The red arrows mark the start and end of the volcanic eruption.

2.5 Geomagnetic and solar activity data

An important factor that impacts the ionosphere and can produce ionospheric scintillation is due to the geomagnetic perturbations and ~~the~~ solar weather. The geomagnetic data used in this study is the planetary index, K_p, which is an internationally recognized index usually used in ~~the~~ aerospace technologies and physical models of the geomagnetic environment. It is obtained from geomagnetic perturbations produced by the solar wind, and it is measured from the K indices of 13 observatories around the world located outside the auroral zone.

The data ~~it~~ is gathered by the GFZ German Research Centre for Geosciences (Matzka et al., 2021), from where it has been downloaded the period corresponding to the la Palma volcanic eruption. The K_p is presented in 3-hour intervals.

The solar activity data has been taken into account by studying the solar flux at the radiofrequency range 10.7 cm (F10.7). The solar flux is one of the main sources of geomagnetic and ionospheric perturbations. Its value is expressed in Solar Flux Units (SFU), and it is recorded with a periodicity of one day from 1947.

The dataset used is the Penticton Solar Radio Flux at 10.7 cm (National Research Council Canada (NRC), 2023), which contains two variables: the observed solar flux at Earth, and the adjusted solar flux, which compensates for the varying distance

from the Sun to the Earth. In our case, the actual flux arriving at the Earth is which is impacting the ionosphere, therefore, the observed flux has been used.

Both geomagnetic disturbances and solar activity data are analyzed in this work in relationship with the scintillation index to complete the study and explain, or discard some signatures found in the ionospheric perturbations.

3 Results and discussion

The three GNSS techniques studied to measure the ionospheric scintillation are correlated to the seismic activity induced by the volcanic eruption. In each of the cases, instantaneous measurements of the S_4 index at every geographic coordinate have been recorded. To integrate this information into something comparable to the integrated energy dissipated by earthquakes, measurements were averaged and integrated into 6-hour segments, corresponding to the same discretization of the earthquake's energy dataset. This 6 h period is long enough to include many measurements and reduce noise, but short enough to allow tracking possible variations within the day.

Figure 15 shows the comparison between the integrated seismic energy by the earthquakes and the different methods to estimate the S_4 ionospheric scintillation index used around La Palma Island. Figure 15a shows the geomagnetic perturbations measured by the planetary index (K_p), and the solar activity represented by the solar flux F10.7. Figure 15b shows the integrated earthquake energy every 6 h interval over a yellow background indicating the time when the eruption was active. Figure 15c shows the ground station data obtained from LPAL and MAS1 stations, and then the percentile 95% computed every 6 h intervals. Figure 15d shows the GNSS-R data from CYGNSS, in the same 6 h intervals. And finally, Fig. 15e shows the GNSS-RO data. The percentile 95% of the S_4 values is shown in these plots after filtering them by distance to the eruption: 300 km in blue color and 1000 km in red color.

A first visual inspection of these data shows a high correlation between the seismic energy and the estimated scintillation. For example, the largest peak in the seismic activity on 3 November at 9 h UTC almost matches with the peaks in the GNSS monitoring ground stations and GNSS-RO measurements, both at the 6-hour interval at 0 h UTC on 4 November. Similarly, the second largest peak in the seismic activity on 17 November at 15 h UTC, has a corresponding replica in the 300 km radius GNSS-RO measurements on 18 November at 0 h UTC.

It can be observed that the GNSS monitoring ground station's data presents an offset between LPAL and MAS1 stations, but they are highly correlated most of the time as both stations can sense the region of the ionosphere likely to be perturbed by the eruptive activity.

Figure 15d shows the CYGNSS GNSS-R data, which represents the least correlated measurement. As mentioned previously, this can be explained as the GNSS-R reflectometry is affected by the sea surface conditions to correctly estimate the ionospheric scintillation index. The red points in Fig. 15d represent S_4 values larger than 0.02 to filter out the values that are more prone to be affected by sea roughness, as explained in Sect. 2.2.
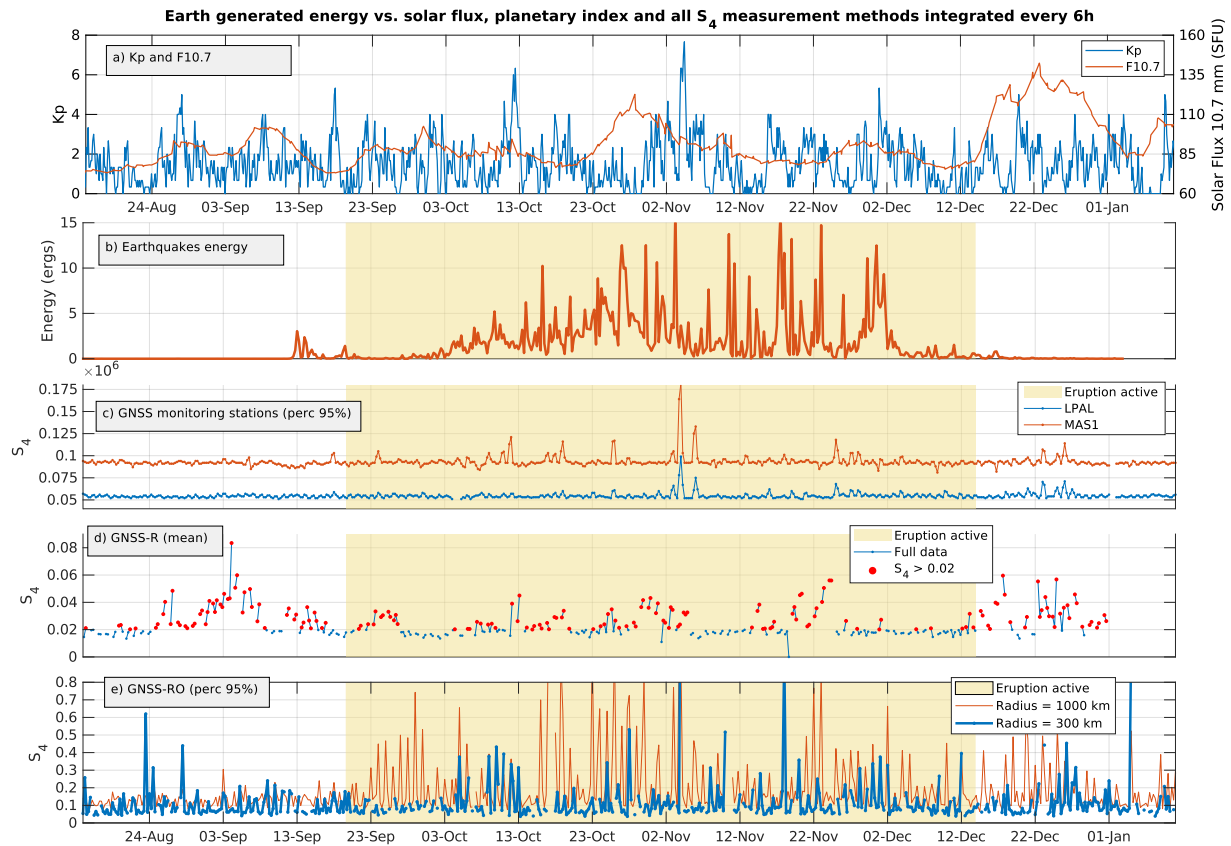
Figure 15. Comparison of a) geomagnetic planetary index and solar flux with b) integrated earthquake's energy every 6 h interval vs. estimated S_4 from the three sources: c) percentile 95 of S_4 obtained from ground stations in La Palma and Maspalomas, d) mean S_4 obtained from CYGNSS GNSS-R, and e) percentile 95% of S_4 obtained from GNSS-RO with two different filtering distances.

Figure 15e shows the GNSS-RO data after being filtered by their distance to the eruption site: 1000 km in a red line ~~,~~ and 300 km in a blue line. The 1000 km one shows more and higher peaks during almost the whole period, which may ~~be indicating~~ indicate that it is being affected by other sources of perturbations, different from the volcanic eruption.

To do a quantitative analysis between the different GNSS data sources, and allow a better comparison of them, a linear correlation between each pair of data (~~earthquakes~~ earthquake energy vs. each of the GNSS measurement methods) has been performed. Before correlating each signal, they have been shifted by a certain amount of time from -10 days to +10 days, in steps of 6 h, equal to the sampling rate for all signals. This way we can also see if the impact of earthquakes in the ionosphere is a precursor or a consequence of it.

After the temporal shift, using the corresponding pair of points (S_4 vs. integrated earthquake energy), a least-squares linear correlation is computed, obtaining for each case its Pearson correlation coefficient, R. Then, for each shifted time, the values

15

of R over time are plotted in Fig. 16. In all cases, the x-axis indicates the amount of time shifted, being negative when the scintillation is a precursor of the earthquakes, and the y-axis is the correlation coefficient R.
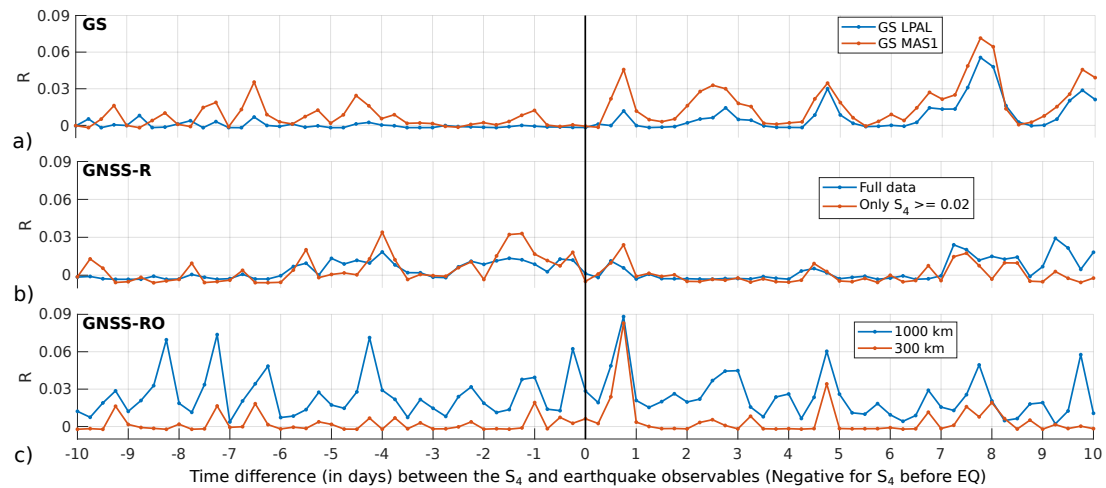

Figure 16. Results of the correlation analysis for each GNSS method and each shifted period in the x-axis: a) GNSS monitoring ground stations, b) GNSS-R data, and c) GNSS-RO data.

~~These results confirm some of the features commented qualitatively in the previous paragraphs. For example, Fig.~~ Figure 16b
proves that the GNSS-R method presents the smallest correlation for all shifting times. Even though, it presents a weak correlation in several points, which tends to be larger when using only the S_4 values larger than 0.02. GNSS-R data present peaks of correlation from -7 to -4 days, also from -2 to +1, and a last ~~set of peaks~~ region of correlation from +7 to +~~10.~~ 10 days.

For GNSS monitoring ground stations data in Fig. 16a the largest peaks of correlation occur when the scintillation is produced around 8 days later, and also 5 or 3 with smaller intensity. Additionally, there is a peak, which is bigger in Maspalomas than in the La Palma monitoring station, at +18 h from the eruption, which supports ~~the fact observed previously in~~ observations from Fig. 15, that the biggest peak in the time series occurs 18 h after the largest earthquake's energy peak.

Figure 16a also shows that the Maspalomas (MAS1) station always has a higher correlation than the La Palma station~~, even if it is on the same island. One~~. A possible explanation for this is that the lower the elevation angle, the larger the detected scintillation is, increasing the possibility of detection of small ionospheric signatures. This is why larger correlations are found in the GNSS-RO measurements.

In the results for GNSS-RO in Fig. 16c it can be seen the largest correlation peak occurs at +18 h after the seismic activity, as for the GNSS monitoring ground stations data. It can also be seen that the data filtered by a 1000 km radius is noisier than the one filtered by a 300 km radius ~~,~~ because the last ones are more related to the eruptive activity than to other external causes. Even though, for the 1000 km radius curve, there are some correlation peaks when the seismic activity precedes the ionospheric perturbations in 8, 7, or 4 days approximately. Also, another peak is found at +4.75 days after the seismic activity, with a smaller replica in the 300 km radius, being the second larger peak for this case.

In Fig. 16, a cross-correlation between two or more techniques is observed sometimes. There are several points that present correlation peaks approximately at the same time interval, reinforcing the results presented and confirming that the different methods can actually detect the same signatures related to ~~the~~ seismic activity.

The same technique has been also applied to correlate the ionospheric scintillation to geomagnetic and space weather indicators: planetary index (K_p), and solar flux (F10.7), respectively. Figure. 17 shows the correlation analysis for the planetary index and the three methods to estimate the S_4: GS, GNSS-R, and GNSS-RO.
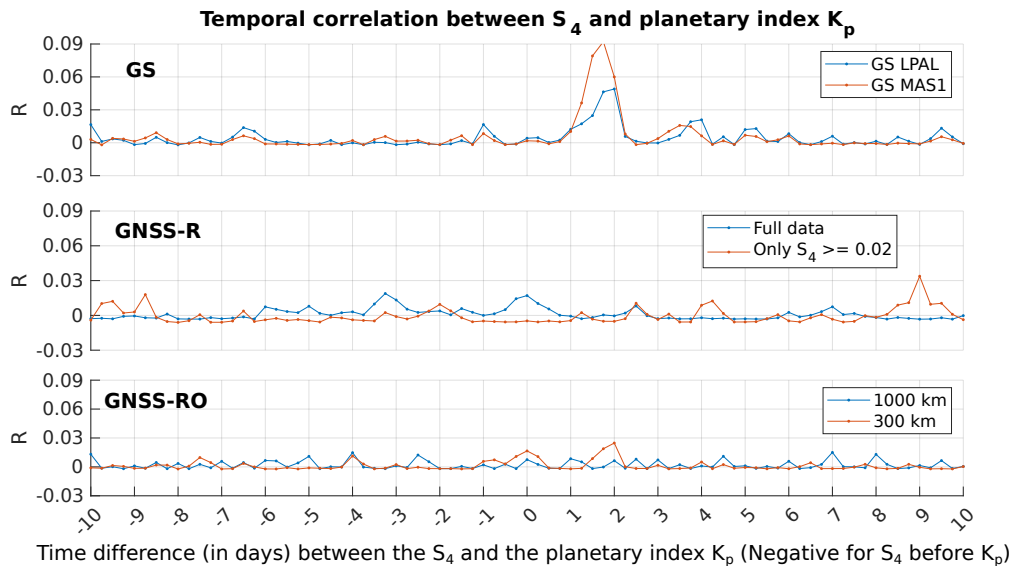

Figure 17. Correlation analysis between the planetary index (K_p) and S_4 from all GNSS methods: a) GNSS monitoring ground stations, b) GNSS-R data, and c) GNSS-RO data.

It can be observed a peak ~~when the EQs occur~~ of correlation when the K_p peaks appear from 1 to 2 days before the S_4 perturbations ~~only in~~ when using the ground station's method. These peaks reach a value of 0.09 for the MAS1 station ~~,~~ and 0.05 for the LPAL station. For the rest of the time windows, the correlation is almost null. The same happens for the GNSS-R and GNSS-RO results, where the correlation is always less than 0.03, and it can be considered negligible.

In Fig. 18 it is shown the result for the correlation between the solar weather variable, F10.7, and the S_4 from each method used. In this case, the solar flux is more correlated with the scintillation when using the GNSS-R method from CYGNSS data, with values up to 0.09. It is less correlated for the ground stations and the GNSS-RO method, being almost zero all the time for the last one.

These last two results ~~indicates~~ indicate that there is a stronger correlation between the ionospheric scintillation and the earthquakes than with solar weather or geomagnetic perturbations. Only in the cases for the GNSS-R compared with the solar flux, and the ground stations with the planetary index, the influence of earthquakes sometimes appears to be smaller than from the space weather variables. This ~~could mean that the influence of earthquakes , is , in general,~~ means that the impact
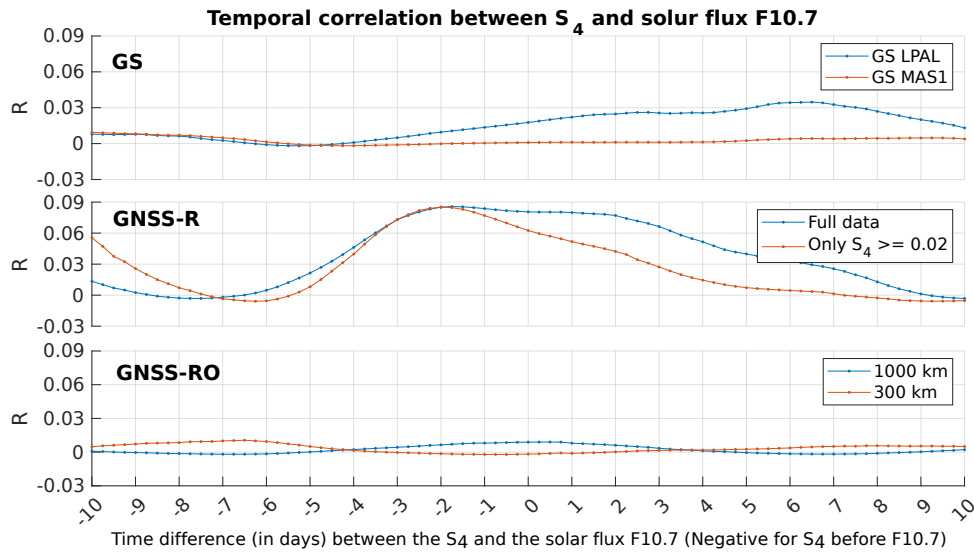
Figure 18. Correlation analysis between the solar flux (F10.7) and S_4 from all GNSS methods: a) GNSS monitoring ground stations, b) GNSS-R data, and c) GNSS-RO data.

285 of earthquakes is locally a stronger factor to perturb the ionosphere. ~~It is clear that the space weather during longer periods of time and wider regions, should be one of the main factors impacting the ionosphere. These results defend the idea~~ These results support the hypothesis that the local perturbations generated by an ~~upcoming~~ impending earthquake can be larger than the ones originated by the solar weather, and can be, therefore, detectable with instruments.

4   Conclusions

290 An analysis of the impacts of the La Palma eruption on ionospheric scintillation has been made by correlating three different ~~ways to measure it by using GNSS signals~~ GNSS datasets (GNSS monitoring ground stations, GNSS-R, and GNSS-RO)~~with the seismic activity related to the eruption~~, relating seismic activity from the eruption to anomalies in the signal.

This allows ~~comparing~~ the comparison between the 3 methods' performance ~~to detect~~ in detecting tiny signals in the iono-sphere produced by seismic activity. A detectable correlation for the GNSS monitoring ground stations, and the GNSS-RO

295 methods is present. The GNSS-R technique resulted in the least favorable technique for this methodology, which may be ex-plained by the rough sea state (SWH > 2 m) for the majority of the observed eruption period. The correlation peaks found in the other two methods are obtained after computing the data for the complete duration of the eruption, from 19 September to 13 December 2021. They show the largest peaks at +18 h after the seismic activity, with a correlation coefficient R of around 0.09 and 0.05 for GNSS-RO and GNSS-GS respectively. ~~Even though they are not very high, they are detectable , and they~~ These

300 detectable correlation signals can be related to the direct energy transfer from the earthquakes to the ionosphere by mechanical gravity waves (pressure waves coupling the atmosphere and the ionosphere), as other studies have reported in other eruptions.

Some correlation has also been found when the earthquakes occur some days before the ionospheric scintillation, mainly in the GNSS-R method, and in the GNSS-RO. In ~~this last one, these peaks occurs~~ GNSS-RO, peaks occur in -4, -7 and -8 days.

In the case of the La Palma volcanic eruption, the pre-earthquake ionospheric perturbations may be produced through a
305 piezoelectric effect caused by the severe seismic activity under La Palma during the whole duration of the eruption. As some studies affirm (Qian et al., 2001), the piezoelectric effect induced by the large underground rocks' pressure can induce electric charges in the surface generating perturbations in the ionosphere's electron density during some days before the earthquakes.

The general conclusion of this study is that the small correlation found between ~~the earthquakes and the~~ earthquakes and ionospheric scintillation using the Pearson coefficient makes it very difficult to use these proxies, at present, in practical
310 applications. This can be due to the small magnitude of the earthquakes associated with this volcanic eruption. Studying earthquakes with higher magnitudes the results may show clearer correlations. The importance of this study is that —to authors' knowledge— the ionospheric scintillation derived from three different GNSS-based methods, namely ground-based monitoring stations, GNSS-RO, and GNSS-R, have been used to analyze ionospheric scintillation and their potential correlation with seismic activity, discarding other sources of geomagnetic activity or space weather events.

References

Angling, M. J., Nogués-Correig, O., Nguyen, V., Vetra-Carvalho, S., Bocquet, F.-X., Nordstrom, K., Melville, S. E., Savastano, G., Mohanty, S., and Masters, D.: Sensing the ionosphere with the Spire radio occultation constellation, Journal of Space Weather and Space Climate, 11, 56, 2021.

Astafyeva, E.: Ionospheric Detection of Natural Hazards, Reviews of Geophysics, 57, 1265–1288, https://doi.org/10.1029/2019rg000668, 2019.

Camps, A., Park, H., Juan, J. M., Sanz, J., González-Casado, G., Barbosa, J., Fabbro, V., Lemorton, J., and Orús, R.: Ionospheric Scintillation Monitoring Using GNSS-R?, in: IGARSS 2018 - 2018 IEEE International Geoscience and Remote Sensing Symposium, pp. 3339–3342, https://doi.org/10.1109/IGARSS.2018.8519088, 2018.

Das, B., Barman, K., Pal, S., and Haldar, P. K.: Impact of Three Solar Eclipses of 2019–2020 on the D-Region Ionosphere Observed From a Subtropical Low-Latitude VLF Radio Station, Journal of Geophysical Research: Space Physics, 127, e2022JA030 353, https://doi.org/https://doi.org/10.1029/2022JA030353, e2022JA030353 2022JA030353, 2022.

De Ragone, A. H., De Manzano, A. N., Elias, A. G., and De Artigas, M. Z.: Ionospheric effects of volcanic eruptions, Geofísica Internacional, 43, 187–192, 2004.

Ding, F., Wan, W., Ning, B., and Wang, M.: Large-scale traveling ionospheric disturbances observed by GPS total electron content during the magnetic storm of 29–30 October 2003, Journal of Geophysical Research: Space Physics, 112, https://doi.org/https://doi.org/10.1029/2006JA012013, 2007.

Fernández, J., Escayo, J., Hu, Z., Camacho, A. G., Samsonov, S. V., Prieto, J. F., Tiampo, K. F., Palano, M., Mallorquí, J. J., and Ancochea, E.: Detection of volcanic unrest onset in La Palma, Canary Islands, evolution and implications, Scientific reports, 11, 1–15, 2021.

Gutenberg, B. and Richter, C.: Magnitude and energy of earthquakes, Nature, 176, 795–795, 1955.

Instituto Geográfico Nacional (IGN): Catálogo de terremotos, https://doi.org/10.7419/162.03.2022, 2022.

Irisov, V., Nguyen, V., Duly, T., Masters, D. S., Nogues-Correig, O., Tan, L., Yuasa, T., and Ector, D. R.: Recent Ionosphere Collection Results From Spire's 3U CubeSat GNSS-RO Constellation, in: AGU Fall Meeting Abstracts, vol. 2018, pp. PA24B–05, 2018.

Jales, P., Esterhuizen, S., Masters, D., Nguyen, V., Correig, O. N., Yuasa, T., and Cartwright, J.: The new Spire GNSS-R satellite missions and products, in: Image and Signal Processing for Remote Sensing XXVI, edited by Bruzzone, L., Bovolo, F., and Santi, E., vol. 11533, p. 1153316, International Society for Optics and Photonics, SPIE, https://doi.org/10.1117/12.2574127, 2020.

Juan, J. M., Aragon-Angel, A., Sanz, J., González-Casado, G., and Rovira-Garcia, A.: A method for scintillation characterization using geodetic receivers operating at 1 Hz, Journal of Geodesy, 91, 1383–1397, https://doi.org/10.1007/s00190-017-1031-0, 2017.

Juan, J. M., Sanz, J., González-Casado, G., Rovira-Garcia, A., Camps, A., Riba, J., Barbosa, J., Blanch, E., Altadill, D., and Orus, R.: Feasibility of precise navigation in high and low latitude regions under scintillation conditions, Journal of Space Weather and Space Climate, 8, A05, https://doi.org/10.1051/swsc/2017047, 2018.

Kamogawa, M.: Preseismic lithosphere-atmosphere-ionosphere coupling, Eos, Transactions American Geophysical Union, 87, 417–424, https://doi.org/https://doi.org/10.1029/2006EO400002, 2006.

Li, G., Ning, B., Zhao, B., Liu, L., Liu, J., and Yumoto, K.: Effects of geomagnetic storm on GPS ionospheric scintillations at Sanya, Journal of Atmospheric and Solar-Terrestrial Physics, 70, 1034–1045, https://doi.org/https://doi.org/10.1016/j.jastp.2008.01.003, 2008.

Liu, J., Chuo, Y., Shan, S.-J., Tsai, Y., Chen, Y.-I., Pulinets, S., and Yu, S.: Preearthquake-ionospheric anomalies registered by continuous GPS TEC, Annales Geophysicae, 22, https://doi.org/10.5194/angeo-22-1585-2004, 2004.

Matzka, J., Bronkalla, O., Tornow, K., Elger, K., and Stolle, C.: Geomagnetic Kp index, https://doi.org/10.5880/KP.0001, 2021.

365   Molina, C. and Camps, A.: First evidences of ionospheric plasma depletions observations using GNSS-R data from CYGNSS, Remote Sensing, 12, 3782, 2020.

Molina, C., Semlali, B. B., Park, H., and Camps, A.: Possible Evidence of Earthquake Precursors Observed in Ionospheric Scintillation Events Observed from Spaceborne GNSS-R Data, in: 2021 IEEE International Geoscience and Remote Sensing Symposium IGARSS, pp. 8680–8683, IEEE, 2021.

370   Molina, C., Boudriki Semlali, B.-E., Park, H., and Camps, A.: A Preliminary Study on Ionospheric Scintillation Anomalies Detected Using GNSS-R Data from NASA CYGNSS Mission as Possible Earthquake Precursors, Remote Sensing, 14, 2555, 2022.

Munoz-Martin, J. F., Perez, A., Camps, A., Ribó, S., Cardellach, E., Stroeve, J., Nandan, V., Itkin, P., Tonboe, R., Hendricks, S., et al.: Snow and ice thickness retrievals using GNSS-R: Preliminary results of the MOSAiC experiment, Remote Sensing, 12, 4038, 2020.

National Research Council Canada (NRC): Solar radio flux - archive of measurements — spaceweather.gc.ca, https://www.spaceweather.gc.
375   ca/forecast-prevision/solar-solaire/solarflux/sx-5-en.php, These data were accessed via the LASP Interactive Solar Irradiance Datacenter (LISIRD) (https://lasp.colorado.edu/lisird/). [Accessed 03-May-2023], 2023.

Puertos del Estado: Conjunto de datos SIMAR, https://bancodatos.puertos.es/BD/informes/INT_8.pdf, 2020.

Puertos del Estado: Predicción de oleaje, nivel del mar. Boyas y mareografos., https://www.puertos.es/en-us/oceanografia/Pages/portus.aspx, access date [23-sep-2022], 2022.

380   Pulinets, S.: Ionospheric Precursors of Earthquakes: Recent Advances in Theory and Practical Applications, Terrestrial Atmospheric and Oceanic Sciences, 15, 413–435, https://doi.org/10.3319/TAO.2004.15.3.413(EP), 2004.

Pulinets, S. and Davidenko, D.: Ionospheric precursors of earthquakes and global electric circuit, Advances in Space Research, 53, 709–723, 2014.

Pulinets, S., Krankowski, A., Hernandez-Pajares, M., Marra, S., Cherniak, I., Zakharenkova, I., Rothkaehl, H., Kotulak, K., Davidenko, D.,
385   Blaszkiewicz, L., et al.: Ionosphere Sounding for Pre-seismic anomalies identification (INSPIRE): Results of the project and Perspectives for the short-term earthquake forecast, Frontiers in Earth Science, 9, 610 193, 2021.

Qian, S.-Q., qi Hao, J., guo Zhou, J., tian Gao, J., ling Wang, M., and Liang, J.: ULF electromagnetic precursors before the 1999 Jiji, Taiwan, earthquake and the comparison with results of simulating experiments, Acta Seismologica Sinica, 14, 342–348, https://doi.org/10.1007/s11589-001-0012-8, 2001.

390   Rodriguez-Alvarez, N., Bosch-Lluis, X., Camps, A., Vall-Llossera, M., Valencia, E., Marchan-Hernandez, J. F., and Ramos-Perez, I.: Soil moisture retrieval using GNSS-R techniques: Experimental results over a bare soil field, IEEE transactions on geoscience and remote sensing, 47, 3616–3624, 2009.

Rovira-Garcia, A., González-Casado, G., Juan, J. M., Sanz, J., and Pérez, R. O.: Climatology of High and Low Latitude Scintillation in the Last Solar Cycle by Means of the Geodetic Detrending Technique, in: Proceedings of the 2020 International Technical Meeting of The
395   Institute of Navigation, Institute of Navigation, https://doi.org/10.33012/2020.17187, 2020.

Shanmugam, S., Jones, J., MacAulay, A., and Van Dierendonck, A.: Evolution to modernized GNSS ionoshperic scintillation and TEC monitoring, in: Proceedings of the 2012 IEEE/ION Position, Location and Navigation Symposium, pp. 265–273, IEEE, 2012.

Shults, K., Astafyeva, E., and Adourian, S.: Ionospheric detection and localization of volcano eruptions on the example of the April 2015 Calbuco events, Journal of Geophysical Research: Space Physics, 121, 10–303, https://doi.org/10.1002/2016ja023382, 2016.

400   Themens, D. R., Watson, C., Žagar, N., Vasylkevych, S., Elvidge, S., McCaffrey, A., Prikryl, P., Reid, B., Wood, A., and Jayachandran, P.:
Global propagation of ionospheric disturbances associated with the 2022 Tonga Volcanic Eruption, Geophysical Research Letters, 49,
e2022GL098 158, 2022.

UCAR/NCAR: UCAR COSMIC Program, 2019: COSMIC-2 Data Products, https://doi.org/10.5065/T353-C093, access date [20-Jun-2022],
2019.

405   Wang, F., Yang, D., and Yang, L.: Retrieval and assessment of significant wave height from CYGNSS mission using neural network, Remote
Sensing, 14, 3666, 2022.

Xu, J., Ke, F., Zhao, X., and Qi, X.: Characteristics of the Ionospheric Disturbances Caused by Typhoon Using GPS and Ionospheric
Sounding, pp. 509–517, https://doi.org/https://doi.org/10.1007/978-981-15-6113-9_57, 2019.

Yong-Qiang, H., Zuo, X., and Dong-He, Z.: Responses of the ionosphere to the Great Sumatra earthquake and volcanic eruption of Pinatubo,
410   Chinese Physics Letters, 23, 1955, 2006.